AGU PUBLICATIONS

JGR

Journal of Geophysical Research: Space Physics

RESEARCH ARTICLE

10.1002/2015JA021568

Simulations of inner radiation belt proton loss during geomagnetic storms

M. A. Engel[1], B. T. Kress[2], M. K. Hudson[1], and R. S. Selesnick[3]

[1]Department of Physics and Astronomy, Dartmouth College, Hanover, New Hampshire, USA, [2]Cooperative Institute for Research in Environmental Sciences, University of Colorado at Boulder, Boulder, Colorado, USA, [3]Space Vehicles Directorate, Air Force Research Laboratory, Kirtland, New Mexico, USA

Key Points:
- Field line curvature scattering by itself is insufficient to explain proton loss in inner belt
- Including the inductive electric field from time stepping TS05 improves particle simulation results
- Inductive electric field does not resolve energy-dependent depth of loss versus HEO data

Correspondence to:
M. A. Engel,
Miles.A.Engel@dartmouth.edu

Citation:
Engel, M. A., B. T. Kress, M. K. Hudson, and R. S. Selesnick (2015), Simulations of inner radiation belt proton loss during geomagnetic storms, *J. Geophys. Res. Space Physics*, *120*, 9323–9333, doi:10.1002/2015JA021568.

Received 12 JUN 2015
Accepted 12 OCT 2015
Accepted article online 15 OCT 2015
Published online 3 NOV 2015

Abstract The loss of protons in the outer part of the inner radiation belt ($L = 2$ to 3) during the 6 April 2000 solar energetic particles event has been investigated using test particle simulations that follow full Lorentz trajectories with both magnetic and electric fields calculated from an empirical model. The electric fields are calculated as inductive fields generated by the time-changing magnetic field, which is achieved by time stepping analytic magnetic fields. The simulation results are compared with proton measurements from the highly elliptical orbit satellite for three different energy ranges (8.5–35 MeV, 16–40 MeV, and 27–45 MeV) as well as previous modeling work done. In previous work, inner zone radiation belt loss during geomagnetic storms has been modeled by simulating field line curvature scattering in static magnetic field snapshots with no electric field. The inclusion of the inductive electric field causes an increase in loss to lower L shells, improving the agreement with the satellite data.

1. Introduction

There is a long history of observations of variation in the outer boundary of the inner zone proton belts [*Blake et al.*, 1992; *Lorentzen et al.*, 2002]. This variability is attributed to geomagnetic activity and often accompanies solar energetic particle events and large-scale restructuring of the magnetic field. Storm time variations in the outer portion of the inner zone radiation belts include the following: radial shifts of preexisting trapped protons, injections of new MeV protons, and loss events [*Selesnick et al.*, 2010]. In this paper we focus on loss events. Several mechanisms for inner ion belt losses during storms have been theorized including the following: hydromagnetic waves [*Dragt*, 1961], low-frequency magnetic fluctuations [*McIlwain*, 1965], perturbation of the boundary of the inner zone [*Gussenhoven et al.*, 1994], and breakdown of adiabatic motion of protons due to magnetic field disturbances [*Anderson et al.*, 1997; *Young et al.*, 2002; *Tu et al.*, 2014]. Because the loss event studied in this paper is correlated to the minimum *Dst* of an accompanying geomagnetic storm, we attribute it to the breakdown of adiabatic motion and subsequent field line curvature scattering (FCS).

FCS occurs when the magnetic field is distorted in such a way to cause the curvature of the field line to be of the same order of magnitude or less than the gyroradius of a proton. This typically occurs when the ring current builds up and causes the field lines to stretch. This stretching results in a smaller curvature which pitch angle scatters protons into the loss cone, leading to a net loss of inner zone protons [*Hudson et al.*, 1997]. While other factors may contribute to the distortion of the magnetic field and FCS, the ring current buildup during geomagnetic storms is the major contributing factor.

Previous work has been done to model satellite data using FCS models [*Selesnick et al.*, 2010; *Zou et al.*, 2011], but there are significant differences between the model results and the observations. *Selesnick et al.* [2010] performed a comparison between losses observed with the highly elliptical orbit (HEO)-3 spacecraft and FCS losses modeled in the *Tsyganenko and Sitnov* [2005] (TS05) geomagnetic field model. HEO-3 is in a highly elliptical orbit with a period of 12 h, perigee of a few hundred kilometers, apogee of roughly 7 R_E, and an inclination of about 63°. The P2, P3, and P4 detectors used in the comparison are omnidirectional and measure energies of 8.5–35 MeV, 16–40 MeV, and 27–45 MeV, respectively. It was found that field line curvature scattering alone was insufficient to explain the losses seen in the data. There are two significant discrepancies between the observed losses and losses modeled with FCS. First, the observed losses extend to lower L shells than in the model results. Second, the FCS model predicts that the minimum L at which losses occur is higher for lower energy particles; however, there is little or no energy dependence apparent in the HEO observations.

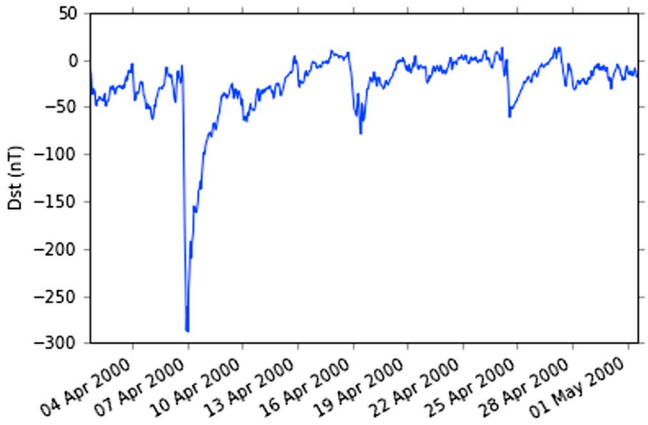

Figure 1. Disturbed storm time field for April 2000.

Zou et al. [2011] performed their comparison between NOAA Polar-Orbiting Environmental Satellite (POES) and the empirical AP8 model. POES is in a near-circular orbit with a radius of approximately 800 km and an inclination of 98°. The POES P7, P8, and P9 detectors are also omnidirectional but cover a much larger range of energies, 35–70 MeV, 70–140 MeV, and 140–500 MeV, respectively. The P7 and P8 energy channels show a depth of loss equivalent to that seen in the HEO data, but P9 shows no loss at any L value. FCS was again shown to be insufficient for modeling the P7 channel but shows good agreement with the P8 and P9 channels, both of which are well above the HEO energy range.

In this paper we resolve some differences between model results and observations by simulating inner zone proton belt losses including the inward and outward radial motions due to ring current changes. Ring current buildup and decay during a geomagnetic storm have a significant impact on the L and energy dependence of the inner zone proton belt, following the storm. If we demand conservation of the first and third adiabatic invariants throughout the storm, (1) drift shells expand radially outward during the main phase, (2) maximum losses occur near minimum *Dst* when field line curvature is greatest, and (3) drift shells move inward during the recovery period. Steps 1 and 3 comprise the *Dst* effect [*Kim and Chan*, 1997], which, combined with loss from FCS, causes a change in the energy-dependent radial profile of inner zone ions between the period of maximum loss and the end of the recovery period. We show that inclusion of these effects has a notable impact on the final state of the inner radiation belt.

In order to examine these effects, an inductive electric field is added to the TS05 geomagnetic field model allowing for particle motion due to the $E \times B$ drift. To test this addition, we use a fully 3-D particle tracing code, with TS05 used for the external field model and International Geomagnetic Reference Field (IGRF) used for the internal field, and the externally calculated inductive electric field. The particles are run from before the onset of the increase in geomagnetic activity to a suitable time after such that the fields have returned to a similar configuration as at the start. The event on 6 April 2000 was chosen to simulate because it was analyzed in both previously mentioned studies and features a large decrease in *Dst* with a steady recovery period (Figure 1). In the following sections we will discuss the methods by which the inductive electric field was calculated, the details of the particle simulations, and the corresponding results of the simulations.

2. Method

Inner zone proton losses are simulated by computing Lorentz trajectories in the TS05 geomagnetic field model. The TS05 model is time dependently driven by measured solar wind, interplanetary magnetic field, and *Dst* input parameters. An important aspect of this work is inclusion of the inductive electric field due to the buildup and decay of the ring current during geomagnetic storms, which creates a time-varying magnetic field. It is shown that this electric field can have a significant effect on the final state of the inner zone proton belt following a loss event. A storm time inductive electric field is obtained from the TS05 field model as in *Ukhorskiy et al.* [2006a, 2006b]. A pure dipole model with a spatially uniform time-varying magnetic field superimposed is also used in this work, as an initial test of the numerical method. Two methods used to obtain the electric field are described below.

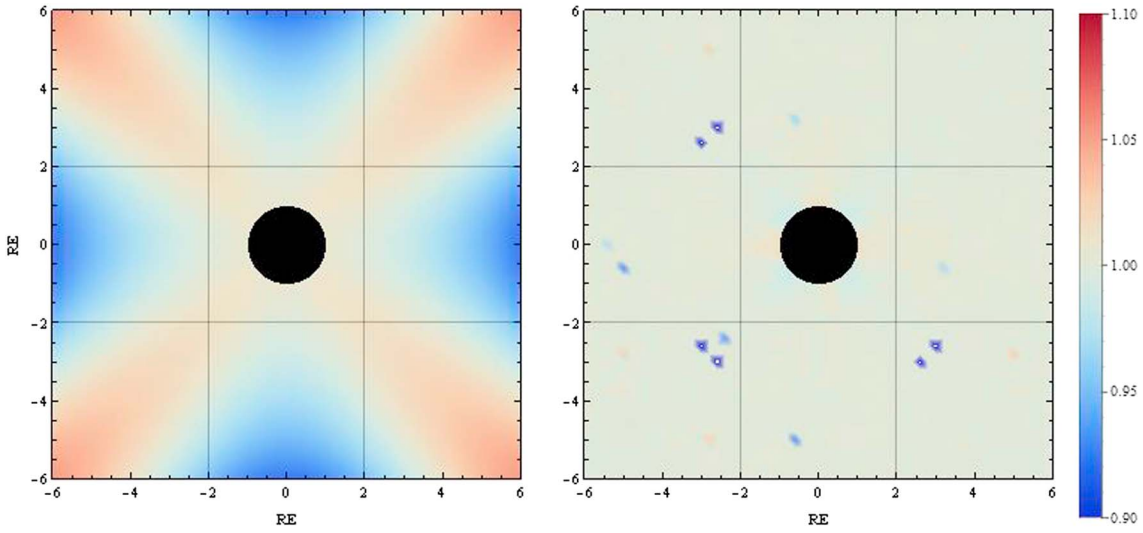

Figure 2. The ratio of the analytic electric field to the model computed electric field for the (left) Biot-Savart method and (right) Euler potential method.

2.1. Calculation of Inductive Electric Field

An inductive electric field is generated any time that you have a time-varying magnetic field. The basic form of this relation is given by Faraday's law

$$\nabla \times \mathbf{E} = -\frac{\partial \mathbf{B}}{\partial t} \tag{1}$$

While this is solvable for any analytic description of the magnetic field with appropriate boundary conditions, numerical solutions, corresponding to $\frac{\triangle \mathbf{B}}{\triangle t}$ obtained from a time dependently driven system, like those from TS05, are more difficult to obtain.

Two methods have been used to numerically solve for the electric field, each with its own advantages. The Biot-Savart method uses a summation over the entire grid (equation (A6)) [*Ukhorskiy et al.*, 2006a, 2006b], making it computationally expensive, but has the advantage of being a straightforward calculation, reliant only on $\nabla \cdot \mathbf{B} = \nabla \cdot \mathbf{E} = 0$. The Euler potential method uses field line tracing to determine the vector potential at each point in space and then computes the electric field (equation (B5)). It is much faster than the Biot-Savart method but relies on the accuracy of the field line tracer, as well as the assumption that $\mathbf{E} \cdot \mathbf{B} = 0$. Detailed calculations for each method can be found in the appendices.

In order to test both of these methods, an analytic, time-changing, magnetic field was created by combining a pure dipole field with a spatially uniform, time-varying, z component magnetic field, so that the full magnetic field equation in Cartesian coordinates is

$$\mathbf{B} = -\frac{3B_0}{r^5} xz\hat{\mathbf{x}} - \frac{3B_0}{r^5} yz\hat{\mathbf{y}} - \left(\frac{B_0}{r^5}(3z^2 - r^2) + B_1(t)\right)\hat{\mathbf{z}} \tag{2}$$

where B_0 is the dipole moment and B_1 is the added uniform field. Using this with equation (1), we can solve for the electric field by assuming a symmetric electric field, centered about the origin, and with $E = 0$ at infinity. This gives us a very simple electric field model:

$$\mathbf{E} = \frac{1}{2}\frac{\partial B_1}{\partial t}(-y\hat{\mathbf{x}} + x\hat{\mathbf{y}}) \tag{3}$$

With this electric field as the analytic solution we can test the validity of the two methods by creating a numerical representation on a grid of the analytic field and then solving for **E** using equations (A6) and (B5). Figure 2 shows an error comparison between model and analytic results for both the Biot-Savart and Euler potential methods, both of which show good agreement.

2.2. Particle Simulations

Following the method outlined in *Kress et al.* [2007], an energetic proton distribution is modeled by following Lorentz trajectories in TS05 magnetic fields and calculated inductive electric fields. Because the energy density of these multi-MeV protons is negligible compared to the thermal population present in the inner radiation belt, we can consider these particles as being noninteracting test particles [*Dessler and Parker*, 1959]. Since the storm time inner zone proton belt losses are believed to be caused by field line curvature scattering, it is necessary to follow the full Lorentz motion of the particle. The test particle trajectories are integrated using a Boris (leapfrog) algorithm, mainly chosen for its explicit conservation of energy [*Birdsall and Langdon*, 2004].

The simulation domain for these particles is limited to a sphere of radius $r = 6\,R_E$, centered on the Earth, with an inner boundary of radius $r = 1\,R_E$. Particles passing either of these boundaries are removed from the simulation. The particles are launched uniformly and randomly from a disk in the equatorial plane at radial distances between 1.8 and 3.8 R_E, energies from 5 to 50 MeV, and equatorial pitch angles between 30 and 90°. Using these parameters, we wish to launch enough particles to fully sample, in an approximately uniform way, the phase space we are examining. The exact form of the energy, pitch angle, and spatial distributions of the test particles is irrelevant, as it is weighted in a postprocessing step.

A numerical detector is used to obtain the modeled particle flux. The detector is a disk in the equatorial plane that counts particles as they pass through and records their position, energy, and equatorial pitch angle. The integration time is chosen such that it is smaller than the smallest particle bounce time, so that we do not oversample any particles with bounce periods shorter than the integration, as compared to those with longer bounce periods. For the work presented here the flux integration periods occur every 10 s and last for 0.1 s. Once all of the particles have been counted, they are binned into L shell, energy, and equatorial pitch angle phase space, giving us a count per bin for each grid point.

As a postprocessing step, a test particle flux is calculated by setting all of the bin weights to one. This test particle flux is then used to compute realistic weights to match an observed or modeled flux distribution. The weighting function is

$$w(L_i, E_j, \alpha_{0_k}) = \frac{j_{\text{modeled}}(L_i, E_j, \alpha_{0_k})}{j_{\text{test particle}}(L_i, E_j, \alpha_{0_k}; t = 0)} \tag{4}$$

where the test particle flux is taken at the start of the run [*Kress et al.*, 2007]. The initial ($t = 0$) flux used in this work is obtained by fitting the observed flux to $j_{\text{modeled}} = e^{-7L_i} E_j^3 \sin^8(\alpha_{0_k})$, which is a fit to the HEO-3 data before the event [*Selesnick et al.*, 2010]. Once these weightings are calculated, they are applied to all grid points at all times, which, for $t = 0$, re-creates the modeled flux, and for all times after creating a suitable simulation flux. Because all of this is done in a postprocessing step, it is possible to test many different initial flux distributions without rerunning any of the particles, which takes the majority of the time in the code. This allows us to test the dependence of the outcome on the initial distribution.

3. Results

In the following paragraphs, particle tracing test results are presented. The results are obtained by following test particle trajectories in TS05 + IGRF magnetic fields, with inductive electric fields calculated using the methods described above. These electric fields were calculated on a grid in solar magnetic coordinates. Because the IGRF (internal) field is rotating with respect to the SM coordinate system, both the inductive electric field due to time-changing solar wind conditions and the inductive portion of the electric field from a rotating nonuniformly magnetized sphere are included [*Kaburaki*, 1980; *Hones and Bergeson*, 1965]. The TS05 model was driven by the data obtained from the Anomalous Composition Explorer spacecraft for the time period from 5 to 8 April 2000. A uniform Cartesian grid with bounds at $-6\,R_E$ and $6\,R_E$ and a resolution of $0.05\,R_E$ was used. In each simulation 2^5 particle trajectories are computed over a 67 h simulated time period. These results are compared against data obtained from the HEO-3 spacecraft.

To understand the effect that the inclusion of an inductive electric field has, the first simulation was done by setting the inductive electric field to zero, so that we could investigate the effect that just the magnetic reconfiguration has on the inner radiation belt. Figure 3 shows the comparison of the starting proton flux to the ending flux, with losses visible in all of the energy channels, although more predominant in the higher

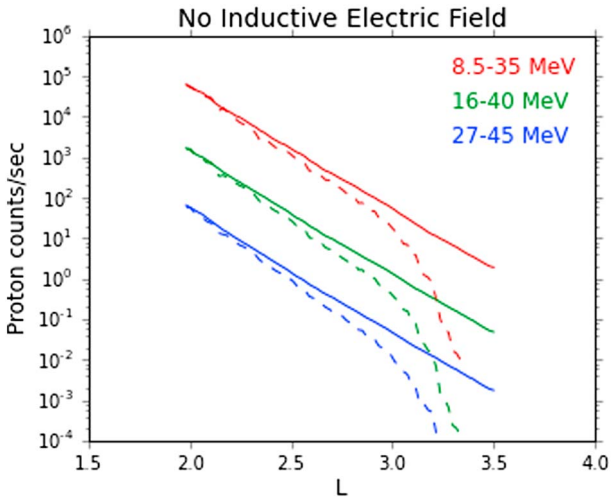

Figure 3. Simulation omnidirectional flux before (solid line) and after (dashed line) event referenced in Figure 1 using no inductive electric field.

energies. This structure of loss is consistent with models that have only looked at field line curvature scattering as a loss mechanism [*Selesnick et al.*, 2010]. From here it is possible to investigate the effect an inductive electric field has on the loss.

Figure 4 shows the comparison of the postevent omnidirectional flux with the inclusion of an inductive electric field, calculated with both the Biot-Savart and Euler potential methods. In both cases you can see that the inward extent of the loss has moved to a smaller L in all of the energy channels. In order to compare the simulated flux results with satellite measurements, it is necessary to understand the method of collection for the data and adjust our simulation as necessary. Both HEO and POES use omnidirectional detectors, but because they are in highly inclined orbits, the pitch angles that are able to reach them are limited. Since our initial modeled flux is peaked at an equatorial pitch angle of 90°, we expect the omnidirectional flux to be dominated by those particles and thus not a good representation of what HEO or POES would see. Figure 5 shows four different plots, each with a range of equatorial pitch angles. We see that for both no electric field (solid) and electric field (dashed) runs, the L at which loss occurs decreases as the equatorial pitch angle is decreased, but in the case of the run with electric field, the change from one pitch angle to another is more dramatic, implying that the inductive electric field has a larger effect on protons with smaller equatorial pitch angles.

By summing the flux for all pitch angles detected by HEO, we compare before and after fluxes for the case of no electric field, and that with the Euler potential-calculated inductive electric field, against the HEO-3 data (Figure 6). The fluxes for both simulation and data are taken at quiet times before and after the storm when the

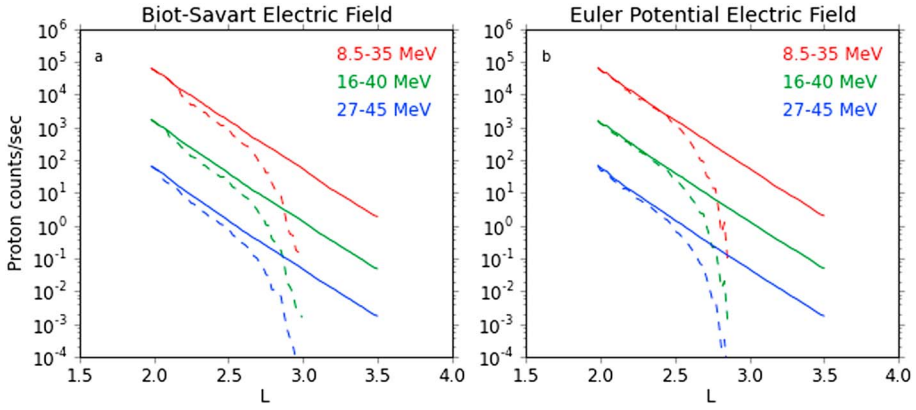

Figure 4. Comparison of the before (solid) and after (dashed) event omnidirectional fluxes for runs with (a) the Biot-Savart-calculated electric field and (b) the Euler potential-calculated electric field.

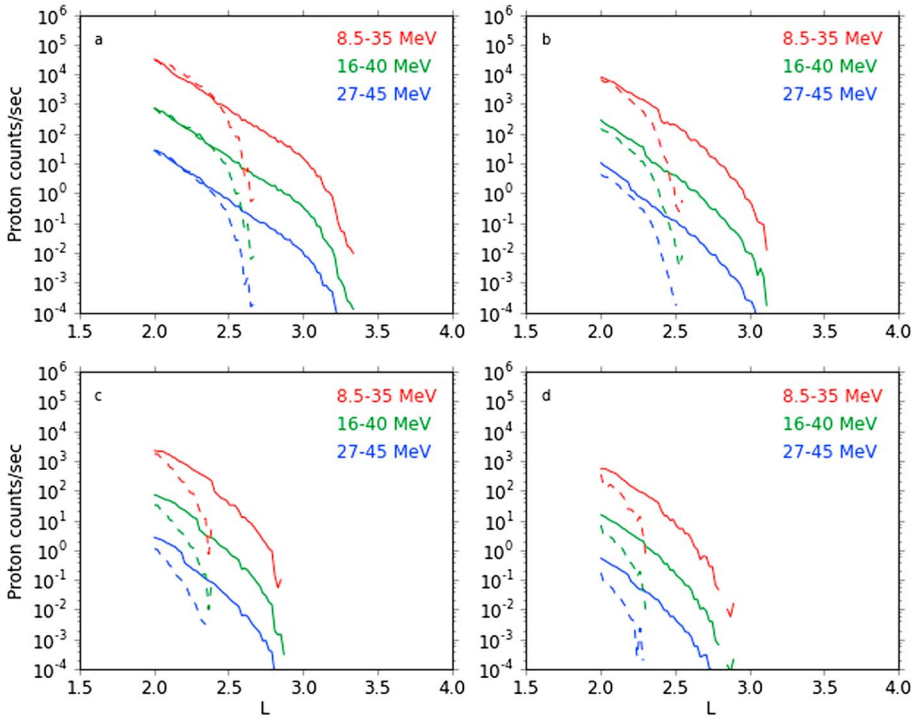

Figure 5. Comparison between runs with no inductive electric field (solid) and the Euler potential-calculated electric field (dashed) of the flux after the event for protons with pitch angles (a) 75–85°, (b) 65–75°, (c) 55–65°, and (d) 45–55°.

flux is relatively steady. This is done so that the time sampling resolution of the HEO spacecraft over various L shells does not diminish the result.

Comparing each case, the inclusion of the inductive electric field improves the agreement with the data in all three energy channels below *L* of 2.5, with the two highest energy channels showing much better agreement between *L* of 2 and 2.5, while the lowest energy channel shows smaller improvements.

Focusing on the middle energy channel (16–40 MeV), Figure 7 shows four plots of flux versus *L* and time covering the entire simulated time. Figures 7a and 7b are with simulated flux averaged over 10 min, while Figures 7c and 7d, simulated flux and HEO data, are averaged over 24 h because of HEO's orbit. Again, the case with no electric field shows little agreement with spacecraft data, while the inclusion of the inductive electric field changes the structure of the spectrograph to include a large, rapid decrease in flux and a slow recovery phase, both of which are evident in the spacecraft data. This plot is included to illustrate the contribution of the *Dst* effect discussed previously. It is important to note that HEO-3 had a data gap at the onset of the storm, thus limiting the amount of data available for this period.

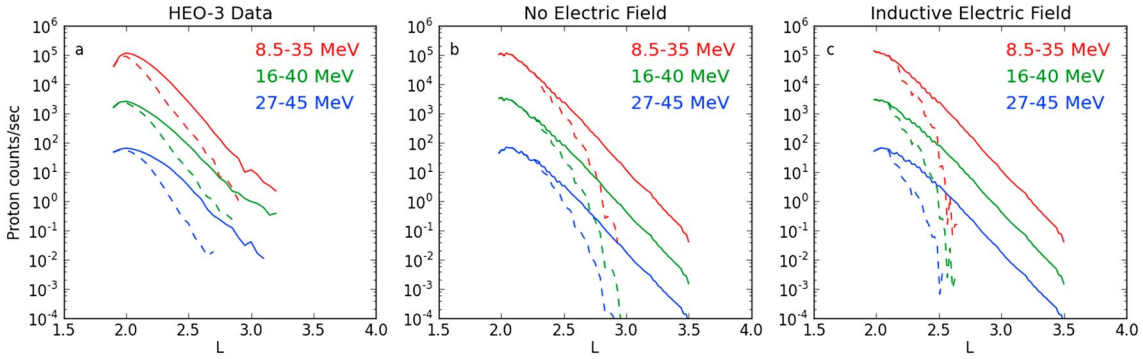

Figure 6. L shell versus flux plots for (a) HEO-3 data, (b) simulation using only TS05, and (c) simulation using TS05 + inductive electric field. The solid line is before the storm, and the dashed line is after the storm, shown in Figure 1.

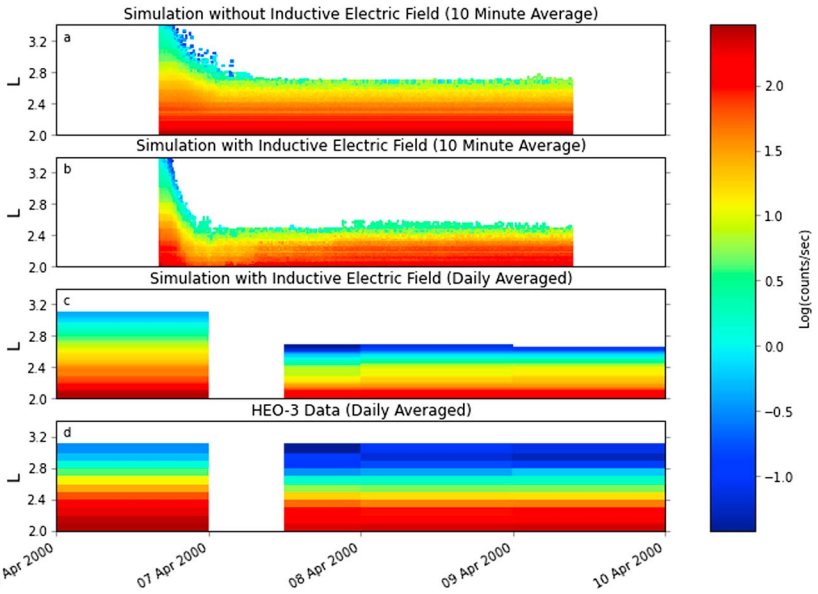

Figure 7. Time versus L shell flux spectrographs for (a) particle simulation with no inductive electric field, (b) particle simulation with inductive electric field, (c) particle simulation with inductive electric field at the same time cadence as the HEO data, and (d) HEO-3 data. The gap in Figures 7c and 7d represents a missing orbit in the HEO data.

4. Discussion and Conclusions

In order to attempt to better simulate the loss of high-energy protons in the inner radiation belt, an inductive electric field generated by the time-varying solar wind conditions and the rotation of the Earth has been calculated. Two methods for calculating the inductive electric field, the Biot-Savart method and Euler potential method, were examined. Both were found to accurately model a known test electric field and so were used to attempt to create an inductive electric field for time-stepped static snapshots of TS05. While both methods are viable ways of calculating an inductive electric field, the Euler potential method is more accurate and faster than the Biot-Savart method when we assume the condition that $\mathbf{E} \cdot \mathbf{B} = 0$, a valid assumption when spatial gradients are large compared with cold plasma gyroradii and timescales of field variations is long compared with gyroperiods.

Comparisons have been made against HEO-3 data using simulations with and without the inductive electric field. The simulations without the inductive electric field show good agreement with the previous theoretical work that has been done [*Selesnick et al.*, 2010] but do not provide good agreement with the HEO-3 data. The inclusion of the inductive electric field moves the depth of loss inward in all three energy channels, improving comparison with HEO-3 data.

We expect the loss to occur principally during the minimum *Dst* when the field lines are most stretched, increasing the curvature. During this time the protons have moved outward to their peak radial distance due to the *Dst* effect and associated inductive electric field. This outward motion is accompanied by a decrease in energy in order to conserve the first adiabatic invariant of the protons, which in turn decreases their gyroradius. Because FCS occurs when the curvature of the field is of the same order of magnitude as the gyroradius, the outward motion has two competing effects. The first, the increase in radial distance, causes the protons to move into an area of increased curvature. While the second, the decrease in energy, causes the gyroradius to decrease. Since the simulation confirms that the largest losses are indeed at the minimum *Dst*, we can say that the first effect is the dominant one for this storm.

For all three energy channels the energy independence that we observed in the data is not present in the simulation. For the two highest energy channels (16–40 MeV and 27–45 MeV) the simulated flux with the inductive electric field seems to agree well with the HEO-3 data flux in terms of shape and depth of loss, but the lowest energy channel (8.5–35 MeV) fails to achieve this same level of agreement. It is possible that the loss at these lower energies is dominated by an energy-dependent effect which is absent from the

presented simulations. Nonetheless, inclusion of the inductive electric field for consistency with a time-varying magnetic field pushed the model-data comparison in the right direction and provides a basis for any future improvement to the model.

Appendix A: Biot-Savart Method

Similar to calculating the magnetic field produced by a current using Ampere's law, $\nabla \times \mathbf{B} = \mu_0 \mathbf{J}$, we can apply the Biot-Savart method, to arrive at an equation for an induced electric field. Starting from Faraday's equation (1), we rewrite it using Green's function formalism.

$$\nabla \times \mathbf{E} = -\frac{1}{4\pi} \int \frac{\partial \mathbf{B}}{\partial t} \nabla^2 \left(\frac{1}{|\mathbf{r} - \mathbf{r}'|} \right) \mathrm{d}^3\mathbf{r}' \tag{A1}$$

Using the identity $\nabla \times \nabla \times \mathbf{A} = \nabla(\nabla \cdot \mathbf{A}) - \nabla^2 \mathbf{A}$, we can rewrite the integral as

$$\nabla \times \mathbf{E} = -\frac{1}{4\pi} \nabla \times \nabla \times \int \frac{\frac{\partial \mathbf{B}}{\partial t}}{|\mathbf{r} - \mathbf{r}'|} \mathrm{d}^3\mathbf{r}' + \frac{1}{4\pi} \nabla \int \frac{\partial \mathbf{B}}{\partial t} \cdot \nabla \left(\frac{1}{|\mathbf{r} - \mathbf{r}'|} \right) \mathrm{d}^3\mathbf{r}' \tag{A2}$$

Integration by parts yields

$$\nabla \times \mathbf{E} = -\frac{1}{4\pi} \nabla \times \nabla \times \int \frac{\frac{\partial \mathbf{B}}{\partial t}}{|\mathbf{r} - \mathbf{r}'|} \mathrm{d}^3\mathbf{r}' + \frac{1}{4\pi} \nabla \int \frac{\nabla \cdot \frac{\partial \mathbf{B}}{\partial t}}{|\mathbf{r} - \mathbf{r}'|} \mathrm{d}^3\mathbf{r}' \tag{A3}$$

With $\nabla \cdot \mathbf{B} = 0$, this simplifies to

$$\nabla \times \mathbf{E} = -\frac{1}{4\pi} \nabla \times \nabla \times \int \frac{\frac{\partial \mathbf{B}}{\partial t}}{|\mathbf{r} - \mathbf{r}'|} \mathrm{d}^3\mathbf{r}' \tag{A4}$$

Solving for $\mathbf{E}$ gives us

$$\mathbf{E} = -\frac{1}{4\pi} \nabla \times \int \frac{\frac{\partial \mathbf{B}}{\partial t}}{|\mathbf{r} - \mathbf{r}'|} \mathrm{d}^3\mathbf{r}' + \nabla \phi \tag{A5}$$

If we assume quasi-neutrality, such that $\nabla \cdot \mathbf{E} = 0$, we can see that $\nabla \phi = 0$, and simplifying this, we arrive at our final equation for the electric field

$$\mathbf{E} = -\frac{1}{4\pi} \int \frac{\frac{\partial \mathbf{B}}{\partial t} \times (\mathbf{r} - \mathbf{r}')}{|\mathbf{r} - \mathbf{r}'|^3} \mathrm{d}^3\mathbf{r}' \tag{A6}$$

Appendix B: Euler Potential Method

Any magnetic field can be written as the cross product of two gradients

$$\mathbf{B} = \nabla \alpha \times \nabla \beta \tag{B1}$$

where α and β are scalar functions. These scalar functions are called Euler potentials [*Stern*, 1967] since $\nabla \alpha \cdot \mathbf{B} = 0$, and so they are constant along the field lines. With the magnetic field defined by the pair of Euler potentials, it is possible to also define a suitable magnetic vector potential which satisfies the equation $\mathbf{B} = \nabla \times \mathbf{A}$; unfortunately, because of gauge invariance and the nonunique nature of the vector potential, care has to be taken to handle the general form.

$$\mathbf{A} = \left(\frac{n}{m} \alpha \nabla \beta - \frac{m-n}{m} \beta \nabla \alpha \right) + \nabla \gamma \tag{B2}$$

Here m and n are arbitrary numbers which define the configuration of the vector potential, and $\nabla \gamma$ represents the gauge invariance. Using this vector potential, we can solve the equation $\mathbf{E} = -\frac{\partial \mathbf{A}}{\partial t} - \nabla \phi$ for the electric field, in terms of the Euler potentials. Simplifying and grouping terms together give us

$$\mathbf{E} = \left(\frac{\partial \alpha}{\partial t} \nabla \beta - \frac{\partial \beta}{\partial t} \nabla \alpha \right) - \nabla \left(\phi + \frac{\partial \gamma}{\partial t} + \frac{n}{m} \alpha \frac{\partial \beta}{\partial t} - \frac{m-n}{m} \beta \frac{\partial \alpha}{\partial t} \right) \tag{B3}$$

which can be rewritten as

$$\mathbf{E} = \left(\frac{\partial \alpha}{\partial t}\nabla\beta - \frac{\partial \beta}{\partial t}\nabla\alpha\right) - \nabla\phi' \tag{B4}$$

where ϕ' is an effective scalar potential. If we then assume the condition that $\mathbf{E}\cdot\mathbf{B} = 0$, which, for a conducting plasma, such as in the radiation belt region, is a good assumption, we can set $\nabla\phi' = 0$, so that our final equation for the inductive electric field is independent of the gauge, scalar potential, and vector potential configurations:

$$\mathbf{E} = \left(\frac{\partial \alpha}{\partial t}\nabla\beta - \frac{\partial \beta}{\partial t}\nabla\alpha\right) \tag{B5}$$

With a working equation for the inductive electric field, the goal becomes finding the needed Euler potentials.

In the pure dipole approximation for the Earth, the Euler potentials can be written as

$$\alpha = \frac{B_0}{r}R_E^3 \sin(\theta)^2 \tag{B6}$$

$$\beta = \phi \tag{B7}$$

where r, θ, and are the standard spherical ϕ coordinates, B_0 is the average magnetic field strength at the equator, and R_E is the radius of the Earth. If we assume our magnetic field to be of an unknown configuration that approaches a pure dipole as we move to the center, then it is possible to trace a field line from any given point inward until the dipole component of the magnetic field dominates. Once there, you can assign the dipole Euler potential to that field line and, since it is constant along field lines, it will correspond to the point at which we started the trace. For this work, however, we have an inner field made up of TS05 and IGRF. Since IGRF is a multipole expansion, the closer we get to the center, the larger it diverges from a pure dipole. For this reason a separate method is needed to be devised to calculate IGRF Euler potentials, so that the aforementioned field line tracing method would still be viable.

Appendix C: Numerical Computation of IGRF Euler Potentials α and β on Spherical Latitude-Longitude Grid

The following is a description of the method used to numerically compute Euler potentials and such that $\mathbf{B} = \nabla\alpha \times \nabla\beta$, where $\mathbf{B}$, is obtained from a degree and order 13 expansion of the IGRF geomagnetic field model. Note that $\mathbf{B}$ is everywhere perpendicular to $\nabla\alpha$ and $\nabla\beta$ and that α and β are constant along field lines. There is considerable freedom on how α and β are chosen. Here we use a method that lends itself to ease of numerical calculation. The method described here is similar to the method used by *Ho et al.* [1997].

As in *Ho et al.* [1997], we define radial grid lines in the equatorial plane 1° apart. The radial lines are at the nodes of an azimuthal grid at $\phi = 0°, 1°, 2°, \ldots, 359°$. Choose $\beta = \phi$ in the *x-y* (equatorial) plane so that $\beta = \phi$ =a constant along each radial line, and $\nabla\beta$ is perpendicular to each line at each point along the line. Since $\nabla\beta$ is also perpendicular to $\mathbf{B}$, and the projection of $\nabla\beta$ onto the *x-y* plane is always in the $+\phi$ direction, the directions of $\nabla\alpha$ and $\nabla\beta$ are thus fixed along the radial grid lines. Also, the magnitude of $\nabla\alpha$ is given by the magnitudes of $\mathbf{B}$ and $\nabla\beta$. The magnitude of α remains arbitrary to an additive constant.

A radial grid in the *x-y* plane is defined, with grid points at $r = r_{\min}, r_{\min} + \mathrm{d}r, r_{\min} + 2\mathrm{d}r, \ldots, r_{\max}$, where $r_{\max}$ sufficiently large that only the dipole term in the IGRF spherical harmonic expansion is significant at radial distances $\geq r_{\max}$. Consider a portion of the equatorial grid shown in Figure C1. The differential area of the annulus sector enclosed by the dashed lines is represented by the vector $\mathbf{ds} = \mathrm{d}r\hat{\mathbf{r}} \times r\mathrm{d}\phi\hat{\phi}$. A numerical method for determining α at each grid point is derived as follows:

$$B \cdot \mathbf{ds} = (\nabla\alpha \times \nabla\beta) \cdot (\mathrm{d}r\hat{\mathbf{r}} \times r\mathrm{d}\phi\hat{\phi}) \tag{C1}$$

$$B_z r\mathrm{d}\phi\mathrm{d}r = (\nabla\alpha \cdot \mathrm{d}r\hat{\mathbf{r}})(\nabla\beta \cdot r\mathrm{d}\phi\hat{\phi}) - (\nabla\alpha \cdot r\mathrm{d}\phi\hat{\phi})(\nabla\beta \cdot \mathrm{d}r\hat{\mathbf{r}}) \tag{C2}$$

$$\nabla\beta \cdot \mathrm{d}r\hat{\mathbf{r}} = 0 \tag{C3}$$

$$B_z r\mathrm{d}\phi\mathrm{d}r = \mathrm{d}\alpha_{\text{along }\hat{\mathbf{r}}}\, d\beta_{\text{along }\hat{\phi}} \tag{C4}$$

$$\frac{\mathrm{d}\alpha}{\mathrm{d}r} = \frac{B_z\, r\, \mathrm{d}\phi}{\mathrm{d}\beta} \tag{C5}$$

$$\Longrightarrow \quad \alpha_i = \alpha_{i+1} - B_z(r_o)\, r_o\, \mathrm{d}r \tag{C6}$$

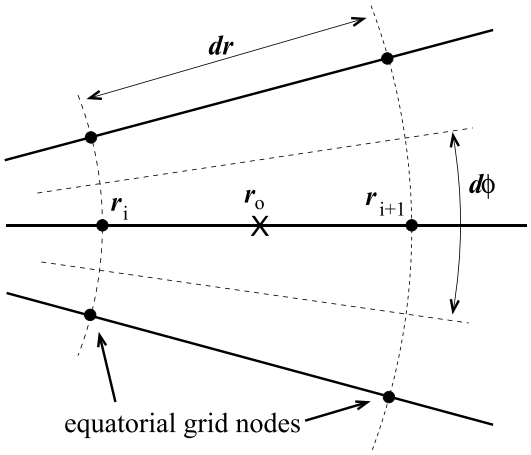

Figure C1. The dashed lines enclose a differential area element in the equatorial plane.

We set $\alpha(r_{max}) = B_0 R_E^3 \sin^2\theta/\alpha$, which, together with $\beta = \phi$, forms an Euler potential pair for an exact dipole. The integration is performed inward along each radial grid line using the last line of equation (C1). The geometric mean $r_o = \sqrt{r_i r_{i+1}}$ is used, which gives the exact result for α in pure dipole field.

Finally, a spherical latitude-longitude grid of desired resolution is defined on a sphere at $r \le r_{min}$. A field line tracing algorithm is used to follow magnetic field lines from positions on the latitude-longitude grid to the equatorial plane. Values of α and β on the latitude-longitude grid are obtained by interpolating α and β from four surrounding grid points in the equatorial plane to the location where the magnetic field line intersects the equatorial plane. We can obtain values of α and β arbitrarily close to the pole of the spherical grid by increasing r_{max}, but we cannot get Euler potentials right at the pole.

In this work, we use the IGRF Euler potentials at $r = r_{min}$ to approximate the sum of IGRF (internal) and TS05 (external) field models. Since the relative contribution to the total field from the external field is smaller at smaller radial distances, r_{min} is chosen small enough so that $|\mathbf{B}_{IGRF}| \gg |\mathbf{B}_{TS05}|$ everywhere on the latitude-longitude grid at $r = r_{min}$.

In general, the accuracy of the method can be improved by adjusting the error tolerance on the field line tracing algorithm and/or by increasing the resolution of the equatorial and latitude-longitude grids. Using $r_{min} = 0.5$, $r_{max} = 256$, and 512 radial grid points, we obtain <1% error between numerical and exact analytic solutions for α in a pure dipole field.

Acknowledgments
This work was supported by the National Science Foundation grant AGS-102333, AGS-1455470 and JHU/APL under NASA prime contract NAS5-01072, with work at Dartmouth supported under ECT (967399) subcontract from UNH. Solar wind parameters are obtained from CDAWeb http://cdaweb.gsfc.nasa.gov. *Dst* data were provided by J.H. King and N. Papatashvilli at ADNET, NASA GSFC, and CDAWeb http://cdaweb.gsfc.nasa.gov. HEO-3 proton data were provided to the Virtual Radiation Belt Observatory (ViRBO) by the Aerospace Corporation http://virbo.org/HEO. Computations were performed on the Dartmouth Discovery Cluster. Support for this work was also provided by the National Science Foundation award ATM-0921979.

References

Anderson, B., R. Decker, N. Paschalidis, and T. Sarris (1997), Onset of nonadiabatic particle motion in the near-Earth magnetotail, *J. Geophys. Res.*, *102*(A8), 17,553–17,569.
Birdsall, C. K., and A. B. Langdon (2004), *Plasma Physics via Computer Simulation*, CRC Press, Boca Raton, Fla.
Blake, J. B., W. Kolasinski, R. Fillius, and E. Mullen (1992), Injection of electrons and protons with energies of tens of MeV into l < 3 on 24 March 1991, *Geophys. Res. Lett.*, *19*(8), 821–824.
Dessler, A. J., and E. N. Parker (1959), Hydromagnetic theory of geomagnetic storms, *J. Geophys. Res.*, *64*(12), 2239–2252.
Dragt, A. (1961), Effect of hydromagnetic waves on the lifetime of Van Allen radiation protons, *J. Geophys. Res.*, *66*(6), 1641–1649.
Gussenhoven, M., E. Mullen, and M. Violet (1994), Solar particle events as seen on CRRES, *Adv. Space Res.*, *14*(10), 619–629.
Ho, C. W., T. S. Huang, and S. Gao (1997), Contributions of the high-degree multipoles of Neptune's magnetic field: An Euler potentials approach, *J. Geophys. Res.*, *102*(A11), 24,393–24,401.
Hones, E. W., and J. E. Bergeson (1965), Electric field generated by a rotating magnetized sphere, *J. Geophys. Res.*, *70*(19), 4951–4958.
Hudson, M., S. Elkington, J. Lyon, V. Marchenko, I. Roth, M. Temerin, J. Blake, M. Gussenhoven, and J. Wygant (1997), Simulations of radiation belt formation during storm sudden commencements, *J. Geophys. Res.*, *102*(A7), 14,087–14,102.
Kaburaki, O. (1980), Determination of the electromagnetic field produced by a magnetic oblique-rotator, *Astrophys. Space Sci.*, *67*(1), 3–18.
Kim, H.-J., and A. A. Chan (1997), Fully adiabatic changes in storm time relativistic electron fluxes, *J. Geophys. Res.*, *102*(A10), 22,107–22,116.
Kress, B., M. Hudson, M. Looper, J. Albert, J. Lyon, and C. Goodrich (2007), Global MHD test particle simulations of > 10 MeV radiation belt electrons during storm sudden commencement, *J. Geophys. Res.*, *112*, A09215, doi:10.1029/2006JA012218.
Lorentzen, K., J. Mazur, M. Looper, J. Fennell, and J. Blake (2002), Multisatellite observations of MeV ion injections during storms, *J. Geophys. Res.*, *107*(A9), 1231, doi:10.1029/2001JA000276.
McIlwain, C. (1965), Redistribution of trapped protons during a magnetic storm, *Space Res.*, *5*, 374–391.
Selesnick, R., M. Hudson, and B. Kress (2010), Injection and loss of inner radiation belt protons during solar proton events and magnetic storms, *J. Geophys. Res.*, *115*, A08211, doi:10.1029/2010JA015247.
Stern, D. (1967), Störmer theory and Euler potentials, *Planet. Space Sci.*, *15*(10), 1525–1530.

Tsyganenko, N., and M. Sitnov (2005), Modeling the dynamics of the inner magnetosphere during strong geomagnetic storms, *J. Geophys. Res.*, *110*, A03208, doi:10.1029/2004JA010798.

Tu, W., M. Cowee, and K. Liu (2014), Modeling the loss of inner belt protons by magnetic field line curvature scattering, *J. Geophys. Res. Space Physics*, *119*, 5638–5650, doi:10.1002/2014JA019864.

Ukhorskiy, A., B. Anderson, K. Takahashi, and N. Tsyganenko (2006a), Impact of ULF oscillations in solar wind dynamic pressure on the outer radiation belt electrons, *Geophys. Res. Lett.*, *33*, L06111, doi:10.1029/2005GL024380.

Ukhorskiy, A., B. Anderson, P. Brandt, and N. Tsyganenko (2006b), Storm time evolution of the outer radiation belt: Transport and losses, *J. Geophys. Res.*, *111*, A11S03, doi:10.1029/2006JA011690.

Young, S., R. Denton, B. Anderson, and M. Hudson (2002), Empirical model for μ scattering caused by field line curvature in a realistic magnetosphere, *J. Geophys. Res.*, *107*(A6), 1069, doi:10.1029/2000JA000294.

Zou, H., Q. G. Zong, G. K. Parks, Z. Y. Pu, H. F. Chen, and L. Xie (2011), Response of high-energy protons of the inner radiation belt to large magnetic storms, *J. Geophys. Res.*, *116*, A10229, doi:10.1029/2011JA016733.